

Generation of quality Green's function libraries in complex three-dimensional crustal structures by adaptive mesh refinement

*Kai Nakao¹, *Hideaki Ito¹, Tsuyoshi Ichimura¹, Kohei Fujita¹, Lalith Wijerathne¹, and Muneo Hori²

¹ Earthquake Research Institute and Department of Civil Engineering, The University of Tokyo, Bunkyo, Tokyo, Japan

{k-nakao, hideakiito, ichimura, fujita, lalith}@eri.u-tokyo.ac.jp

² Research Institute for Value-Added-Information Generation, Japan Agency for Marine-Earth Science and Technology, Yokohama, Kanagawa, Japan
horimune@jamstec.go.jp

Abstract. Fault slip estimation from crustal deformation is essential for understanding earthquake mechanisms, and three-dimensional subsurface models have become incorporated in the estimation to account for the geometric and material heterogeneity in the crust. In the estimation process, a precomputed Green's function library (GFL), which represents the displacement field due to unit point loads at each receiver on ground surface, can be employed for computing arbitrary source responses through convolution of the source terms and the GFL. However, challenges remain in generating meshes adapted to the singularity of the point loads and in assessing the accuracy of the GFL. We developed a GFL computation method, Adaptive Finite Element Method for Green's Function Library (AFEM-GFL). By combining initial meshes with good element quality and a mesh refinement algorithm that is resistant to element quality degradation, our method can generate meshes well adapted to computing GFLs. The accuracy of the results is assessed through convergence of the solution and comparisons between the convergent solutions from different initial meshes. In numerical experiments on a two-layered half-space and a realistic crustal structure of Japan, accurate and convergent GFLs were obtained with moderate amount of computational resources in the settings where it was difficult to achieve with uniform meshes even using a massively parallel supercomputer. These quality GFLs will serve as a robust foundation for reliable fault slip estimation.

Keywords: Green's function library · Adaptive finite element method · Crustal structure

1 Introduction

Estimation of coseismic fault slip based on crustal deformation is crucial for deepening our understanding of earthquake mechanisms and assessing disaster

*Kai Nakao and Hideaki Ito equally contributed to this work.

risks. In the estimation, it is common to model the crust as a flat and homogeneous semi-infinite elastic medium [12] and estimate parameters of the fault model that can reproduce the observed crustal deformation. On the other hand, geometric and material heterogeneity in the crust should be considered in cases where the subsurface structure is complex. Attempts have been made to construct a three-dimensional subsurface structure model that can properly represent these features and employ numerical crustal deformation simulations by the finite element method or the spectral element method as the forward analysis in the estimation process[6]. When there is a nonlinear relationship between the fault model parameters and crustal deformation, the computational cost for the estimation can be huge performing costly numerical simulations every time the parameters are updated in the optimization process. In such cases, methods that reduce the computational costs utilizing the reciprocity theorem [5] are effective. According to the reciprocity theorem, the displacement observed at a receiver point on the ground surface due to a load applied at a subsurface source point is equal to the displacement observed at the source point due to a load applied at the receiver point. A fault slip can be approximated as a set of forces at several points in numerical simulations. If we precompute a set of the subsurface displacement field due to unit point loads applied at each receiver point on the ground surface, which we call a Green's Function Library (GFL), the displacement on the ground surface due to arbitrary fault slips can be obtained by convolution of the source terms and the GFL without performing simulations.

Challenges in constructing GFL for 3D subsurface structures include the quantitative evaluation of the accuracy of the GFL and the generation of high-quality meshes. In finite element analysis of crustal deformation due to fault slips, it is known that the size of the elements near the fault affects the accuracy of the solution [9]. Similarly, the accuracy of the GFL is expected to be affected by the elements near the loading points on the surface. Therefore, it is desirable to generate GFL using methods that allow verification of sufficiency of the mesh resolution based on the quantitative evaluation. Moreover, realistic crustal structures often have thin layers with complex geometry near the ground surface. When controlling the mesh size to refine the elements around the loading points, it is challenging to generate meshes that accurately represent the geometry while maintaining good element quality (i.e., avoiding elements with high aspect ratio) when using general-purpose mesh generators.

To address the aforementioned challenges, we developed a method to generate GFL, which we call Adaptive Finite Element Method for Green's Function Library (AFEM-GFL). Adaptive finite element method (AFEM) is a technique that iteratively conducts finite element analysis, estimates the error, and refines the mesh based on the error to accurately compute fields with significant variations [1]. In AFEM-GFL, algorithms that can protect the layers geometry and are resistant to element quality degradation are employed for initial mesh generation and mesh refinement. This allows for the generation of high-quality meshes well adapted for the computation of GFLs. Regarding the accuracy evaluation for the GFLs, the convergence of the solution can be assessed from the difference

of the solutions between subsequent iterations. Furthermore, inadequate mesh quality could lead to convergent but inaccurate solutions. By comparing solutions obtained from runs with different initial meshes, it is possible to detect if any significant issues that affect the accuracy of the GFLs arise during the mesh refinement. The GFL, whose quality is assured from these evaluations, can be a robust foundation for the reliable fault slip estimation.

This paper describes the details of the AFEM-GFL method in Section 2 and demonstrates its effectiveness through numerical experiments computing GFL for a simple two-layered half-space and a realistic crustal structure of Japan in Section 3. A summary of this study is provided in Section 4.

2 Method: AFEM-GFL

This section describes the details of the developed GFL computation method, AFEM-GFL. As shown in Algorithm 1, AFEM-GFL generates n different initial meshes, and GFLs are obtained by adaptive mesh refinement starting from each of them, then accuracy of them is evaluated. In this study, we assume $n = 2$ for the number of initial meshes, but it can be increased to three or more to ensure robustness. Within this framework, by employing initial meshes with fine resolution and good element quality, along with a mesh refinement strategy that is resistant to element quality degradation, high-quality adaptive meshes can be generated even for crustal structures with complex geometries. The degrees of freedom tend to be large from the early stages in this approach, and that large cost is handled by parallelizing the computation by MPI. Below, we explain the details of each step in Algorithm 1.

Algorithm 1 AFEM-GFL

```

1: Generate  $n$  initial meshes (2.1).
2: for mesh in (mesh1, mesh2,  $\dots$ , mesh_ $n$ ) do *
3:   for  $i = 1, \dots, i_{\max}$  do
4:     Compute GFL by finite element method (2.2).
5:     Estimate posterior error for each element (2.3).
6:     Refine mesh as indicated by error estimator (2.4).
7:   end for
8: end for
9: Evaluate accuracy of GFLs (2.5).
10: if the accuracy is not sufficient then
11:   Improve initial mesh quality and go to *
12: end if

```

2.1 Generation of initial meshes

When targeting models with complex layer structures, generating the initial meshes is not straightforward. In this study, we utilize the mesh generation algo-

rithm by Ichimura et al. (2009) [7], which can produce meshes that can properly represent complex layer structures with good element quality. This algorithm covers the entire domain with cubic background cells, and approximate the geometry of the layers for each cell to avoid generating elements with high aspect ratios, then decompose the domain into tetrahedral elements. Furthermore, this approach can form an octree structure of background cells, allowing it to hierarchically merge cells, thus reducing the number of elements in regions distant from the layer boundaries.

This method takes two parameters: ds , which is the side length of the background cells, and nk , which controls the largest merged cell size, $ds \times 2^{nk-1}$. If ds is too large, the approximation of the geometry of the layers may become too coarse. In AFEM-GFL, whether ds is sufficiently small that this approximation does not significantly affect the GFLs can be checked based on the accuracy evaluation described in Section 2.5. Also, excessive merging of cells may result in leaving inadequately refined regions in the mesh. nk is set to one or two in this study.

2.2 Computation of GFL

To calculate the displacement fields by loading in x , y , and z directions at each loading point on the top surface of the model, the following governing equation is discretized and solved by the finite element method in the semi-infinite domain:

$$\nabla \cdot \sigma + \mathbf{f}_c = \mathbf{0}. \quad (1)$$

Here, σ is the stress tensor, and \mathbf{f}_c is the body force equivalent to a point load:

$$\mathbf{f}_c = \mathbf{s}\delta(\mathbf{x} - \boldsymbol{\xi}), \quad (2)$$

where \mathbf{s} is the load vector and $\boldsymbol{\xi}$ is the loading point. Each component of stress tensor can be expressed in terms of the displacement as

$$\sigma_{ij} = \lambda\delta_{ij}\frac{\partial u_k}{\partial x_k} + \mu\left(\frac{\partial u_i}{\partial x_j} + \frac{\partial u_j}{\partial x_i}\right) \quad (3)$$

where λ and μ are Lamé parameters, and δ_{ij} is the Kronecker delta. Discretizing the equation using a set of basis functions, solving Eq. (1) reduces to solving the following linear equation:

$$\mathbf{K}\mathbf{u} = \mathbf{f}. \quad (4)$$

Here, \mathbf{K} is the stiffness matrix, and \mathbf{u} and \mathbf{f} are nodal displacement and force vectors, respectively. Specifically, \mathbf{f} has non-zero values only for components corresponding to nodes in elements that contain $\boldsymbol{\xi}$. To better represent the infinite conditions with a smaller computational domain, infinite elements are implemented on the sides and bottom of the model [8]. The adaptive conjugate gradient method [3] is used to solve Eq. (4). When there are M loading patterns, we obtain the GFL $\{\mathbf{u}_i \mid 1 \leq i \leq M\}$ by solving Eq. (4) for each corresponding nodal forces $\mathbf{f}_i (i = 1, \dots, M)$.

2.3 Posterior error estimation

Based on the results of finite element analysis, posterior error estimation is performed for each element, and those predicted to have large errors are targeted for refinement. In this study, we employ the posterior error estimator for elasticity problems proposed by Vefürth (1999) [14]. Once the displacement field \mathbf{u}_h is determined, the posterior error estimator η_K for element K is given by:

$$\eta_K = \left\{ h_K^2 \|R_K(\mathbf{u}_h)\|_K^2 + \sum_{E \in \mathcal{E}_K} \frac{1}{2} h_E \|R_E(\mathbf{u}_h)\|_E^2 \right\}^{\frac{1}{2}}. \quad (5)$$

Here, h_K and h_E are the diameters of element K and face E , respectively, and \mathcal{E}_K is the set of faces comprising K . $R_K(\mathbf{u}_h)$ and $R_E(\mathbf{u}_h)$ denote the residuals at K and E , respectively. These residuals are defined as:

$$R_K(\mathbf{u}_h) = \int_K \|\nabla \cdot \sigma(\mathbf{u}_h) + \mathbf{f}_c\|^2 dV \quad (6)$$

$$R_E(\mathbf{u}_h) = \begin{cases} \int_E \|J_E(\mathbf{n}_E \cdot \sigma(\mathbf{u}_h))\|^2 dS & \text{if } E \in \mathcal{E}_\Omega \\ 0 & \text{otherwise} \end{cases}, \quad (7)$$

where J_E and \mathbf{n}_E are the jump operator and normal vector on E , respectively. \mathcal{E}_Ω is the set of faces which are not on the boundary of the model. However, for elements containing the loading points, the singularity of \mathbf{f}_c makes it difficult to compute $R_K(\mathbf{u}_h)$. In such cases, η_K is not computed, and those elements are always selected for refinement. In the computation of GFL, M posterior error estimators η_K^i ($i = 1, \dots, M$) are obtained corresponding to the M loading patterns. From these, we define the following metric: $\tilde{\eta}_K = \max_i \eta_K^i / \bar{u}_K^i$. Here, \bar{u}_K^i is the average displacement norm for loading pattern i at nodes in the element K . Normalizing the error estimator by the displacement aims to mitigate locally large errors near the loading points. The elements satisfying $\tilde{\eta}_K > \theta \tilde{\eta}_{\max}$ are selected for refinement, where $\tilde{\eta}_{\max}$ is the maximum value of $\tilde{\eta}_K$ among elements not containing the loading points, and θ is a threshold value set to 0.01 in this study.

2.4 Mesh refinement

In mesh refinement, the selected elements are subdivided into smaller elements. In refining the unstructured meshes for complex geometries, a highly robust algorithm must be used, capable of preserving the representation of the layer structures while maintaining good element quality. In this study, we refine the mesh by tetrahedral bisection. Tetrahedral bisection involves adding a new node at the midpoint of an edge of the target tetrahedron to divide it into two tetrahedra, and dividing tetrahedra containing hanging nodes into multiple tetrahedra. By choosing bisecting edges according to the algorithm proposed by Arnold & Mukherjee (1999) [2], it is analytically guaranteed that this process yields a conforming mesh when repeated a finite number of times, providing high robustness

for the complex geometries. Furthermore, it is ensured that the shapes of the generated tetrahedra are closed to a finite set of shape patterns determined by the original tetrahedron, supporting that this method is resistant to element quality degradation. Protection of the layer structures is achieved by inheriting the properties of each original tetrahedron to the ones generated by bisection.

Additionally, smoothing of the mesh is performed to locally improve the quality of the elements generated by bisection. The nodes of the newly generated elements and their neighbors are moved according to

$$\mathbf{P}_i^{\text{new}} = \mathbf{P}_i^{\text{old}} + \frac{\lambda}{|N_i|} \sum_{j \in N_i} (\mathbf{P}_{i,j} - \mathbf{P}_i^{\text{old}}) \quad (8)$$

until the maximum aspect ratio of those elements stops decreasing. In Eq. (8), $\mathbf{P}_i^{\text{old}}$ and $\mathbf{P}_i^{\text{new}}$ denote the positions of node i before and after the move, respectively, while $\mathbf{P}_{i,j}$ is the position of node j which is adjacent to node i . N_i represents the set of nodes adjacent to node i , and λ is a small constant. The nodes are moved in the direction of the average position of their neighbors to mitigate the degradation of element quality by bisection. To prevent destruction of the layer structures, the smoothing is performed only for nodes not on the layer boundaries.

2.5 Accuracy evaluation of GFLs

Although the accuracy of the solutions can be predicted by the error estimator η_K , it cannot be calculated for elements containing the loading points. Consequently, mesh refinement does not necessarily lead to a reduction in η_K for all the elements. For a more direct accuracy evaluation, displacements are sampled at several points in the model, and used to calculate accuracy metrics.

As an indicator of convergence of the GFL, the following d_j^i is defined:

$$d_j^i = \frac{1}{M} \sum_{l=1}^M \frac{\sqrt{\sum_{k=1}^3 (u_{j,k,l}^i - u_{j,k,l}^{i-1})^2}}{\sqrt{\sum_{k=1}^3 (u_{j,k,l}^{i-1})^2}}. \quad (9)$$

Here, $u_{j,k,l}^i$ is the k -th component of the displacement at the sampling point j for loading pattern l obtained on the mesh after i -th refinement. The convergence of d_j^i for all j as i increases indicates that the sampled displacements are converging. d_j^i can be calculated for each of GFL obtained on mesh1 and mesh2.

In cases where inadequately refined regions remain in the mesh, extremely poor quality elements are generated, or the approximation of the layer structures is too coarse, d_j^i approaching zeros might indicate convergence of the GFL to incorrect solutions. To detect such situations, the following e_j^i is defined:

$$e_j^i = \frac{1}{M} \sum_{l=1}^M \frac{\sqrt{\sum_{k=1}^3 (u_{j,k,l}^{i1} - u_{j,k,l}^{i2})^2}}{\sqrt{\sum_{k=1}^3 (u_{j,k,l}^{i1})^2}}. \quad (10)$$

Here, $u_{j,k,l}^{i1}$ and $u_{j,k,l}^{i2}$ are the displacements sampled from GFLs on mesh1 and mesh2, respectively. The convergence of e_j^i for all j as i increases indicates that the convergent GFLs are consistent between mesh1 and mesh2. In such a situation, it is evaluated that no issues that distort the sampled displacements have occurred during the mesh refinement process, and high-accuracy GFLs have been obtained. If e_j^i remains large and does not decrease in the iterative mesh refinement process, it is necessary to improve the quality of the initial meshes and rerun AFEM-GFL.

3 Numerical Experiments

In this section, we describe the numerical experiments targeting a two-layered half-space and a realistic crustal structure in Japan. Section 3.1 discusses a numerical experiment where the response due to point loads at a single point on the top surface of the two-layered half-space is computed by AFEM-GFL. Through this experiment, we demonstrate AFEM-GFL's capability to compute displacements in high accuracy in terms of the metrics d_j^i and e_j^i , and examine how the mesh refinement progresses and how the response converges. Section 3.2 discusses a numerical experiment for a realistic crustal structure in Japan, where GFL is obtained by computing responses due to loads at multiple points and crustal deformation at the loading points is computed using the obtained GFL. Through this experiment, we demonstrate that AFEM-GFL is also effective for analysis targeting models with complex geometries and that high-accuracy crustal deformation can be computed from the obtained GFL.

3.1 Two-layered half-space

For a model consisting of two horizontal layers with different material properties, we computed the response due to loads at a single point on the top surface of the model. The layer structure and point load settings are shown in Table 1, with an overview of the model shown in Fig. 1. We denote the settings where the initial mesh was generated with $(ds, nk) = (1.4 \text{ km}, 2)$ and $(2.8 \text{ km}, 1)$ as AFEM-GFL1 and AFEM-GFL2, respectively. This numerical experiment involved 15 iterations of mesh refinement for both AFEM-GFL1 and AFEM-GFL2. For calculating the metrics d_j^i and e_j^i , displacements were sampled at 1575 points within the range $22.4 \text{ km} \leq x, y \leq 380.8 \text{ km}$, $179.2 \text{ km} \leq z \leq 254.8 \text{ km}$.

Table 1. Settings for the two-layered half-space model

Domain size	$0 \text{ km} \leq x, y \leq 403.2 \text{ km}$
Layer 1	$(E, \nu) = (2.89 \text{ GPa}, 0.44)$, $250.176 \text{ km} \leq z \leq 260.176 \text{ km}$
Layer 2	$(E, \nu) = (23.6 \text{ GPa}, 0.26)$, $0 \text{ km} \leq z \leq 250.176 \text{ km}$
Loading Point	$(203.338 \text{ km}, 203.448 \text{ km}, 260.176 \text{ km})$
Loads	$(1 \text{ N}, 0 \text{ N}, 0 \text{ N}), (0 \text{ N}, 1 \text{ N}, 0 \text{ N}), (0 \text{ N}, 0 \text{ N}, 1 \text{ N})$

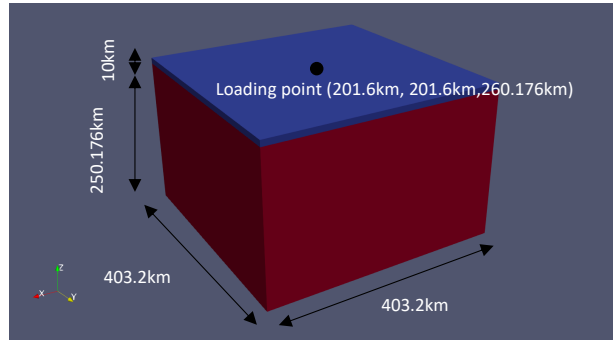


Fig. 1. Overview of the two-layered half-space model and the loading point.

Fig. 2 shows the mesh refinement process. Fig. 2(a) displays only the elements subjected to tetrahedral bisection, illustrating that refinement initially occurred around the loading point and spread over the domain after the mesh around the loading point was refined. Fig. 2(b) shows the mesh after 15 iterations of refinement.

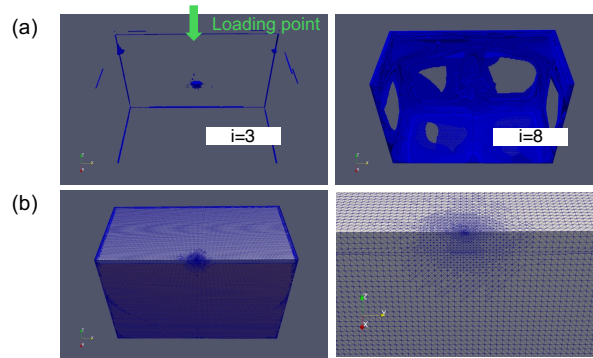


Fig. 2. (a) Elements subjected to refinement during the 3rd and 8th iterations. (b) Mesh after 15 refinements for AFEM-GFL2 model, cut at $x = 201.6$ km, showing the side containing $x = 0$ km. The left panel shows the overview and the right panel shows a close-up view around the loading point.

d_j^i was computed from the sampled displacements and its distribution is presented in Fig. 3(a). The maximum value of d_j^i at $i = 15$ is 0.014% and 0.028% for AFEM-GFL1 and AFEM-GFL2, respectively, indicating that displacements were converged through mesh refinement. Similarly, e_j^i was computed and its distribution is shown in Fig. 3(b). At $i = 15$, the value of e_j^i is confined to 0.050%.

It implies that convergent displacements for AFEM-GFL1,2 are consistent, suggesting that high accuracy of the solutions obtained by AFEM-GFL.

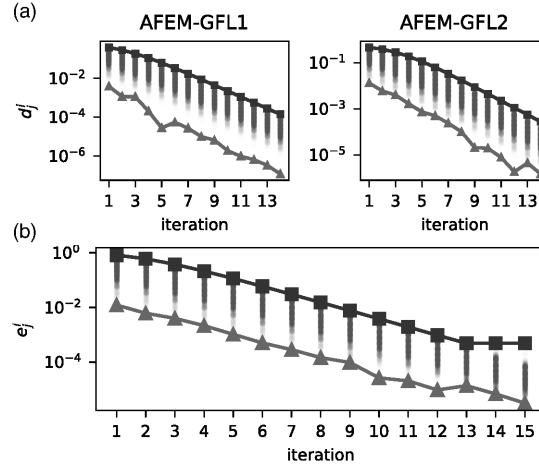


Fig. 3. (a) Distribution of d_j^i for AFEM-GFL1 and AFEM-GFL2. (b) Distribution of e_j^i . In both figures, the value of each metric at each sample point is shown as a dot, with square and triangle markers representing maximum and minimum values, respectively.

Mainly two patterns for convergence of the displacements were observed. Fig. 4 presents examples of each pattern, compared with displacements computed using three meshes with uniform element sizes of 2.8 km, 1.4 km, and 0.7 km. At sample points far from the loading point, as shown in Fig. 4(a), the AFEM-GFL1 and AFEM-GFL2 results converged to the same value and the size of the element containing the loading point has a dominant effect on the convergence. For sample points near the loading point, as shown in Fig. 4(b), the two solutions converged to slightly different values. However, as indicated by the metric e_j^i , these differences are small.

We compare the computational cost of analysis using the uniform mesh 0.7km and AFEM-GFL1 in Table 2. The degrees of freedom for the AFEM-GFL1's final mesh is no more than 1/100 of that for the uniform mesh 0.7km. Further significant refinement would be required to achieve convergence with uniform meshes and such analysis would necessitate even larger computational resources, while high-accuracy convergent solutions were achieved with moderate-scale computer cluster (320 CPU cores) by AFEM-GFL. This result highlights the attractiveness of the method in terms of capability computing, although the total elapsed time for it was large due to the repetitive finite element analyses and the mesh refinement process.

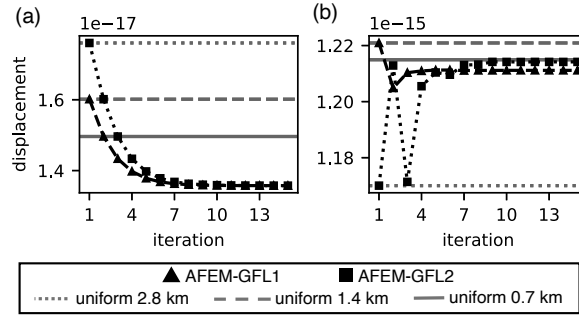


Fig. 4. y components of the displacement due to a load in x direction at sample points are shown. (a) Displacement at (89.6 km, 89.6 km, 201.6 km). (b) Displacement at (201.6 km, 201.6 km, 254.8 km).

Table 2. Comparison of the uniform mesh 0.7km and AFEM-GFL1. Supercomputer Fugaku[13] and a Xeon Gold 6230-based CPU cluster were used for uniform 0.7 km and AFEM-GFL1, respectively. The elapsed time for the uniform mesh includes the time for mesh generation, partitioning, and finite element analysis. One for AFEM-GFL1 includes, in addition to the above, the time for error estimation and mesh refinement.

	Processor	# of CPU cores	Elapsed time(hour)	DoF
Uniform 0.7km	A64FX	38400	2.6	9.9×10^8
AFEM-GFL1	Xeon Gold 6230	320	22.3	7.3×10^6

3.2 Crustal structure in Japan

Numerical experiments were conducted for a model of the crustal structure in the Tohoku region of Japan. The Japan Integrated Velocity Structure Model (JIVSM) [10], a unified underground structure model of the Japanese islands, provides a Digital Elevation Model (DEM) representing the layer structure in the form of (latitude, longitude, elevation) and material properties of each layer. We utilized these data to generate the crustal structure model. DEM data for the longitude range $139.7^\circ\text{E} \sim 142.7^\circ\text{E}$ and latitude range $37.4^\circ\text{N} \sim 39.4^\circ\text{N}$ were extracted from the JIVSM, and too thin layers near the ground surface was deleted [11], then converted to a Cartesian coordinate system [6] to obtain a DEM in the range of $0 \leq x \leq 240$ km, $0 \leq y \leq 200$ km, $0 \leq z \leq 206$ km. Using this data, meshes generated with the settings $(ds, nk) = (0.625$ km, 2) and $(1.25$ km, 1) were used as initial meshes for AFEM-GFL1 and AFEM-GFL2 settings, respectively, and 15 iterations of mesh refinement were performed for both settings. Three loading patterns of $(1\text{ N}, 0\text{ N}, 0\text{ N})$, $(0\text{ N}, 1\text{ N}, 0\text{ N})$, $(0\text{ N}, 0\text{ N}, 1\text{ N})$ were applied to each of the 16 points evenly distributed on the surface within the range 93 km $\leq x \leq 172$ km, 78 km $\leq y \leq 144$ km. Displacements sampled at 350 points within the range of 60 km $\leq x \leq 180$ km, 60 km $\leq y \leq 140$ km, 40 km $\leq z \leq 195$ km were used to evaluate d_j^i and e_j^i . Fig. 5 presents an overview of the model and loading points.

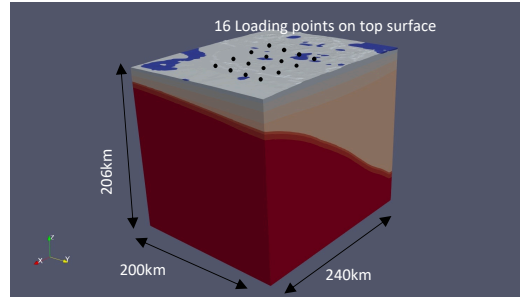


Fig. 5. Overview of the crustal structure model and the loading points.

Fig. 6 shows the mesh refinement process. In Fig. 6(a), only the elements subjected to tetrahedral bisection are displayed, showing a similar trend to the setting in Section 3.1 where refinement initially focuses on the loading points and then spreads over the domain. Fig. 6(b) shows the final mesh for AFEM-GFL2. The maximum aspect ratios in the final meshes for AFEM-GFL1 and AFEM-GFL2 are 36.6 and 36.2, respectively, while those in the initial meshes are 8.85 and 8.64. Although the maximum aspect ratio increased around 4 times during mesh refinement, no degenerate elements (e.g., aspect ratio greater than 1000) were generated even for the crustal structure model.

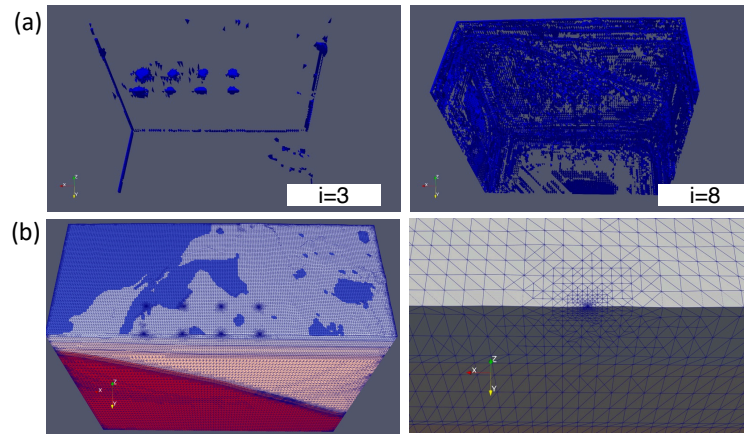


Fig. 6. (a) Elements subjected to refinement during the 3rd and 8th iterations. (b) Mesh after 15 refinements for AFEM-GFL2 model, cut at $y = 120$ km, showing the side containing $y = 0$ km. The left panel shows the overview and the right panel shows a close-up view around the loading point at $x = 93.4$ km, $y = 100.0$ km.

Regarding the accuracy of the computed GFLs, Figs. 7(a) and (b) show the distribution of d_j^i and e_j^i , respectively. For d_j^i , the maximum values at $i = 15$ are 0.02% and 0.04% for AFEM-GFL1 and AFEM-GFL2, respectively. As for e_j^i , the maximum value was 0.60% at $i = 15$. This confirms that even when targeting complex structure models, accurate GFL can be computed by AFEM-GFL from the perspective of d_j^i and e_j^i . However, compared to the setting in Section 3.1, the reduction of e_j^i stopped earlier, and the residual of e_j^i after 15 iterations was larger. One reason might be that while the geometry of the layer structure was accurately represented by the mesh in the two-layered half-space model, it was approximated when generating the initial mesh for the crustal structure model. Although the algorithm used in this study cannot improve geometry representation through mesh refinement, using such methods that correct geometries referring the original DEM when adding nodes during tetrahedral bisection may potentially reduce e_j^i further.

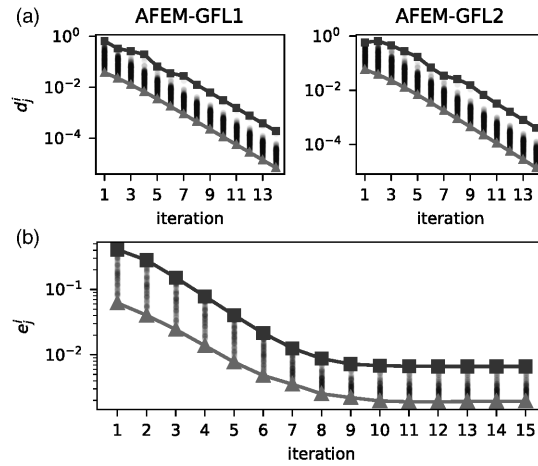


Fig. 7. (a) Distribution of d_j^i for AFEM-GFL1 and AFEM-GFL2. (b) Distribution of e_j^i . In both figures, the value of each metric at each sample point is shown as a dot, with square and triangle markers representing maximum and minimum values, respectively.

Furthermore, the accuracy of crustal deformation computed from the obtained GFLs was also evaluated. Here, we calculated the displacements at the 16 loading points due to a point source at position (62 km, 102 km, 162 km) with a moment tensor of $m_{xx} = m_{yy} = m_{zz} = m_{xy} = m_{yz} = 0, m_{zx} = 1.0 \times 10^{19} \text{ N} \cdot \text{m}$. The point source was approximated as a set of forces acting on vertices of a cube with a side length of 5 km [4], and displacement was obtained by calculating the convolution with the GFLs. Similar to the metrics in equations (9) and (10), the

accuracy of point source response was evaluated using metrics defined as follows:

$$\tilde{d}_j^i = \frac{\sqrt{\sum_{k=1}^3 (u_{j,k}^i - u_{j,k}^{i-1})^2}}{\sqrt{\sum_{k=1}^3 (u_{j,k}^{i-1})^2}} \quad (11)$$

$$\tilde{e}_j^i = \frac{\sqrt{\sum_{k=1}^3 (u_{j,k}^{i1} - u_{j,k}^{i2})^2}}{\sqrt{\sum_{k=1}^3 (u_{j,k}^{i1})^2}}. \quad (12)$$

Here, in Eq. (11), $u_{j,k}^i$ represents the k -component of the point source response at the loading point j obtained using the GFL after i -th refinement. In Eq. (12), $u_{j,k}^{i1}$ and $u_{j,k}^{i2}$ represent the responses obtained using the GFL in AFEM-GFL1 and AFEM-GFL2 settings, respectively. The distribution of \tilde{d}_j^i and \tilde{e}_j^i are shown in Figs. 8(a) and (b), respectively. The maximum values of \tilde{d}_j^i at $i = 15$ is 0.0008% for AFEM-GFL1 and 0.001% for AFEM-GFL2, confirming that the point source response was converged as well as the GFL. As for \tilde{e}_j^i , the maximum value is 0.79% at $i = 15$, confirming that the two responses from AFEM-GFL1 and AFEM-GFL2 are aligned. Evaluating the accuracy of the GFLs at the source point, the maximum value of e_j^{15} is 0.2%. The order of magnitude of the maximum value of e_j^{15} and \tilde{e}_j^{15} is consistent, suggesting that the point source responses were computed with a similar level of accuracy as the GFLs. In this study, the accuracy of the source response is evaluated with the source representation fixed, but future works should consider the impact of the source representation (e.g., the size of the cube for the point source).

4 Conclusion

In this study, we presented a method called AFEM-GFL for calculating GFLs using adaptive mesh refinement with the quantitative accuracy evaluation of solutions. This method generates adaptive meshes suitable for GFL calculations even for models with complex layer structures and allows the quantitative evaluation of accuracy from the perspectives of solution convergence and consistency of solutions obtained from different initial meshes.

Numerical experiments on a two-layered half-space confirmed that high-accuracy convergent solutions can be obtained using this method, as both metrics \tilde{d}_j^i and \tilde{e}_j^i became small. While a convergent solution could not be obtained even with 9.9×10^8 degrees of freedom using a uniform mesh, the degrees of freedom in the final mesh of AFEM-GFL were 7.3×10^6 , enabling execution on a moderate scale computer cluster. This feature shows the superiority of the proposed method over analysis using uniform meshes, although the elapsed time for AFEM-GFL was longer than analysis using uniform meshes. In numerical experiments targeting the realistic crustal structure model, it was confirmed that

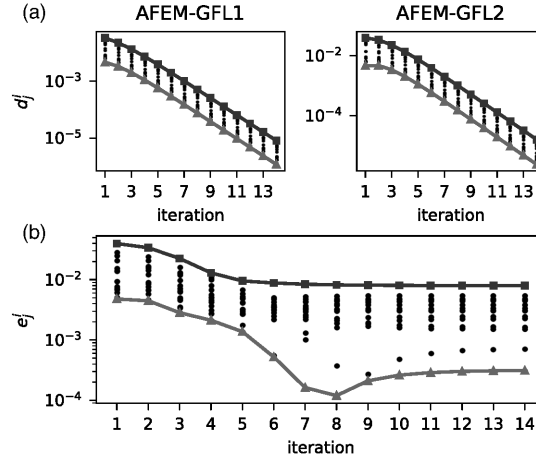


Fig. 8. (a) Distribution of $\tilde{d}_j^{\tilde{}}$ for AFEM-GFL1 and AFEM-GFL2. (b) Distribution of $\tilde{e}_j^{\tilde{}}$. In both figures, the value of each metric at each sample point is shown as a dot, with square and triangle markers representing maximum and minimum values, respectively.

this method is robust, assuring a certain level of accuracy even for models with the complex geometry. It was also verified that point source responses can be calculated with similar accuracy to that of the obtained GFLs.

We can obtain quality GFLs using the proposed method. Those will be utilized for reliable source estimation and enhancing our understanding of earthquakes.

CRedit authorship contribution statement **Kai Nakao**: Investigation, Methodology, Software, Visualization, Writing - original draft **Hideaki Ito**: Investigation, Methodology, Software, Visualization, Writing - original draft **Tsuyoshi Ichimura**: Conceptualization, Funding acquisition, Methodology, Project administration, Supervision, Writing - original draft, Writing - review & editing **Kohei Fujita**: Conceptualization, Supervision, Writing - review & editing. **Lalith Wijerathne**: Conceptualization, Supervision, Writing - review & editing. **Muneo Hori**: Conceptualization, Writing - review & editing.

Acknowledgments. This work was supported by MEXT, Japan as “ Program for Promoting Researches on the Supercomputer Fugaku ” (Large-scale numerical simulation of earthquakes by Fugaku supercomputer, JPMXP1020230213). This work was supported by JSPS KAKENHI, Japan Grant Numbers 23H00213, 22K18823. This work used computational resources of Fugaku provided by the RIKEN Center for Computational Science (Project ID: hp230203, hp240217). This work was supported by JST SPRING, Grant Number JPMJSP2108.

Disclosure of Interests. The authors have no competing interests to declare that are relevant to the content of this article.

References

1. Adjerid, S., Flaherty, J.E.: A local refinement finite-element method for two-dimensional parabolic systems. *SIAM Journal on Scientific and Statistical Computing* **9**(5), 792–811 (1988). <https://doi.org/10.1137/0909053>
2. Arnold, D.N., Mukherjee, A.: *Tetrahedral Bisection and Adaptive Finite Elements*, pp. 29–42. Springer New York, New York, NY (1999). https://doi.org/10.1007/978-1-4612-1556-1_2
3. Golub, G.H., Ye, Q.: Inexact preconditioned conjugate gradient method with inner-outer iteration. *SIAM Journal on Scientific Computing* **21**(4), 1305–1320 (1999). <https://doi.org/10.1137/S1064827597323415>
4. Graves, R.W.: Simulating seismic wave propagation in 3d elastic media using staggered-grid finite differences. *Bulletin of the Seismological Society of America* **86**(4), 1091–1106 (08 1996). <https://doi.org/10.1785/BSSA0860041091>
5. Graves, R.W., Wald, D.J.: Resolution analysis of finite fault source inversion using one- and three-dimensional green's functions: 1. strong motions. *Journal of Geophysical Research: Solid Earth* **106**(B5), 8745–8766 (2001). <https://doi.org/10.1029/2000JB900436>
6. Hori, T., Agata, R., Ichimura, T., Fujita, K., Yamaguchi, T., Inuma, T.: High-fidelity elastic green 's functions for subduction zone models consistent with the global standard geodetic reference system. *Earth, Planets and Space* **73** (12 2021). <https://doi.org/10.1186/s40623-021-01370-y>
7. Ichimura, T., Hori, M., Bielak, J.: A hybrid multiresolution meshing technique for finite element three-dimensional earthquake ground motion modelling in basins including topography. *Geophysical Journal International* **177**(3), 1221–1232 (06 2009). <https://doi.org/10.1111/j.1365-246X.2009.04154.x>
8. Ichimura, T., Agata, R., Hori, T., Hirahara, K., Hori, M.: Fast numerical simulation of crustal deformation using a three-dimensional high-fidelity model. *Geophysical Journal International* **195**(3), 1730–1744 (09 2013). <https://doi.org/10.1093/gji/ggt320>
9. Kim, M., So, B.D., Kim, S., Jo, T., Chang, S.J.: Mesh size effect on finite source inversion with 3-d finite-element modelling. *Geophysical Journal International* **237**(2), 716–728 (02 2024). <https://doi.org/10.1093/gji/ggae060>
10. Koketsu, K., Miyake, H., Suzuki, H.: Japan integrated velocity structure model version 1. In: *Proceedings of the 15th World Conference on Earthquake Engineering*. p. 1773 (09 2012)
11. Murakami, S., Hashima, A., Inuma, T., Fujita, K., Ichimura, T., Hori, T.: Detectability of low-viscosity zone along lithosphere–asthenosphere boundary beneath the nankai trough, japan, based on high-fidelity viscoelastic simulation. *Earth, Planets and Space* **76** (06 2024). <https://doi.org/10.1186/s40623-024-02008-5>
12. Okada, Y.: Surface deformation due to shear and tensile faults in a half-space. *Bulletin of the Seismological Society of America* **75**(4), 1135–1154 (08 1985). <https://doi.org/10.1785/BSSA0750041135>
13. RIKEN Center for Computational Science: Supercomputer fugaku, <https://www.rccs.riken.jp/en/fugaku/>
14. Verfürth, R.: A review of a posteriori error estimation techniques for elasticity problems. *Computer Methods in Applied Mechanics and Engineering* **176**(1), 419–440 (1999). [https://doi.org/10.1016/S0045-7825\(98\)00347-8](https://doi.org/10.1016/S0045-7825(98)00347-8)